Atmos. Chem. Phys. Discuss., 15, 20679–20708, 2015
www.atmos-chem-phys-discuss.net/15/20679/2015/
doi:10.5194/acpd-15-20679-2015
© Author(s) 2015. CC Attribution 3.0 License.

Atmospheric Chemistry and Physics Discussions

This discussion paper is/has been under review for the journal Atmospheric Chemistry and Physics (ACP). Please refer to the corresponding final paper in ACP if available.

Sensitivity of simulated CO_2 concentration to sub-annual variations in fossil fuel CO_2 emissions

X. Zhang[1,2], K. R. Gurney[1], P. Rayner[3], D. Baker[4], and Y.-P. Liu[5]

[1]School of Life Science, Arizona State University, Tempe, AZ, USA
[2]College of Science, San Diego State University, San Diego, CA, USA
[3]Earth Sciences, University of Melbourne, Melbourne, Australia
[4]Cooperative Institute for Research in the Atmosphere, Colorado State University, Fort Collins, USA
[5]Laboratory for Atmosphere, Science Systems and Applications, Inc., NASA Goddard Space Flight Center Code 614 Greenbelt, USA

Received: 8 July 2015 – Accepted: 18 July 2015 – Published: 31 July 2015

Correspondence to: X. Zhang (tyouxia@gmail.com)

Published by Copernicus Publications on behalf of the European Geosciences Union.

Abstract

Recent advances in fossil fuel CO_2 ($FFCO_2$) emission inventories enable sensitivity tests of simulated atmospheric CO_2 concentrations to sub-annual variations in $FFCO_2$ emissions and what this implies for the interpretation of observed CO_2. Six experiments are conducted to investigate the potential impact of three cycles of $FFCO_2$ emission variability (diurnal, weekly and monthly) using a global tracer transport model. Results show an annual $FFCO_2$ rectification varying from −1.35 to +0.13 ppm from the combination of all three cycles. This rectification is driven by a large negative diurnal $FFCO_2$ rectification due to the covariation of diurnal $FFCO_2$ emissions and diurnal vertical mixing, and a smaller positive seasonal $FFCO_2$ rectification driven by the covariation of monthly $FFCO_2$ emissions and monthly atmospheric transport. The diurnal $FFCO_2$ emissions are responsible for a diurnal $FFCO_2$ concentration amplitude of up to 9.12 ppm at the grid cell scale. Similarly, the monthly $FFCO_2$ emissions are responsible for a simulated seasonal CO_2 amplitude of up to 6.11 ppm at the grid cell scale. The impact of the diurnal $FFCO_2$ emissions, when only sampled in the local afternoon is also important, causing an increase of +1.13 ppmv at the grid cell scale. The simulated CO_2 concentration impacts from the diurnally and seasonally-varying $FFCO_2$ emissions are centered over large source regions in the Northern Hemisphere, extending to downwind regions. This study demonstrates the influence of sub-annual variations in $FFCO_2$ emissions on simulated CO_2 concentration and suggests that inversion studies must take account of these variations in the affected regions.

1 Introduction

Quantification of the spatial and temporal distribution of carbon sources and sinks is critical for projecting future atmospheric CO_2 concentrations and climate change (Field et al., 2007). Inferring exchanges of CO_2 between the atmosphere and the terrestrial biosphere/ocean from atmospheric CO_2 observations, using inverse methods based

ACPD
15, 20679–20708, 2015

on atmospheric transport models, has been an important approach (e.g., Tans et al., 1990; Enting, 2002; Gurney et al., 2002).

In atmospheric CO_2 inversions, fossil fuel CO_2 ($FFCO_2$) emissions are often treated as a known quantity in the system; consequently, uncertainty in $FFCO_2$ emissions is not considered explicitly and errors in the distribution of simulated atmospheric $FFCO_2$ are translated into errors in the terrestrial biospheric flux estimates. This problem has not been well-studied, due mainly to limitations such as the coarse resolution of traditional $FFCO_2$ inventories, the sparse monitoring of atmospheric CO_2 concentrations, and sub-grid parameterization of atmospheric transport models. In recent years, significant advances have been made in increasing the density of atmospheric observations and in the accuracy, fidelity and resolution of $FFCO_2$ inventories. For example, the network of atmospheric high-frequency CO_2 concentration measurements has grown over the last decade (NACP project in North America and CarboEurope_IP project in Europe). Global $FFCO_2$ inventories have been produced at high resolution in both the space and time domains – these resolve the CO_2 emissions at spatial scales smaller than 10 km and with hourly time resolution (Rayner et al., 2010; Oda and Maksyutov, 2011; Wang et al., 2013; Nassar et al., 2013; Asefi-Najafabady et al., 2014). These advances provide information that permits a careful examination of how the high-resolution $FFCO_2$ emission data products impact the spatial and temporal distribution of atmospheric CO_2 and flux estimates (Ciais et al., 2009; Gurney et al., 2005; Peylin et al., 2011; Nassar et al., 2013; Asefi-Najafabady et al., 2014). Further, the development of atmospheric transport models with increased spatial and temporal resolution makes it possible to quantify these impacts (e.g., Kawa et al., 2010; Peylin et al., 2011). Previous literature reported the uncertainty in related inversion and forward simulation studies (Gurney et al., 2005; Peylin et al., 2011; Nassar et al., 2013). For example, Gurney et al. (2005) investigated the impact of monthly-varying $FFCO_2$ emissions on inverted net carbon exchange and found a monthly bias of up to 50 % in biospheric net fluxes in some places caused by unaccounted-for variations in fossil fuel emissions.

ACPD
15, 20679–20708, 2015

Peylin et al. (2011) showed a seasonal uncertainty of about 2 ppm in simulated CO_2 concentration associated with uncertainty in the

spatial and temporal variability of $FFCO_2$ emissions over Europe. Similarly, Nassar et al. (2013) reported the impact of time-varying $FFCO_2$ emissions on selected geographical regions during wintertime. Previous studies, however, focused on only one or two components of the sub-annual $FFCO_2$ cycles, or else on limited spatial regions or time periods. Thus, a complete exploration of the space/time influence of all sub-annual variations of $FFCO_2$ across the globe is needed.

Inversion analysis infers the distribution of sources and sinks of CO_2 by reconciling the observed global atmospheric CO_2 concentrations at a network of sampling stations with simulated CO_2 concentrations obtained by driving an atmospheric transport model with an initial estimate of CO_2 fluxes. During this process, the interaction of temporally-varying boundary CO_2 fluxes with atmospheric transport/mixing has been shown to impact the inferred surface CO_2 source/sink distribution. For example, the covariation of seasonal/diurnal biospheric fluxes and seasonal/diurnal atmospheric transport causes a significant seasonal/diurnal effect (commonly called the rectifier) on CO_2 concentrations, even if the fluxes at each grid cell average to zero across each time period (e.g., Keeling et al., 1989; Denning et al., 1995, 1996; Yi et al., 2004; Chen et al., 2004; Chan et al., 2008; Williams et al., 2011). The biospheric rectification is characterized by a time-mean CO_2 spatial concentration gradient, with the diurnal effect at local-to-regional scales caused by the interaction of diurnal biospheric fluxes with the diurnal variation of vertical mixing in the planetary boundary layer (PBL), and the seasonal rectifier effect at the global scale resulting from the interaction of seasonal biospheric fluxes with seasonal atmospheric transport. By contrast, few studies have quantified the rectification of atmospheric CO_2 concentration associated with the sub-annual variations of $FFCO_2$ fluxes (diurnal, weekly and monthly).

In this paper, we test the sensitivity of simulated global atmospheric CO_2 concentration to sub-annual temporal variations in $FFCO_2$ emissions using a tracer transport model. The sub-annual $FFCO_2$ emission variability is comprised of three cyclic com-

ACPD
15, 20679–20708, 2015

ponents: diurnal, weekly, and seasonal. The resulting surface atmospheric CO_2 concentration from these individual components and their sum are compared to simulated CO_2 concentrations driven by a "flat" (temporally invariant) $FFCO_2$ emissions inventory. The impact on the column-integral simulated CO_2 concentration is also examined.

The structure of this paper is as follows: Sect. 2 describes the $FFCO_2$ emissions and sub-annual variability, the biospheric fluxes used for comparison with the $FFCO_2$ emissions, the atmospheric tracer transport model employed in model simulations, and the methods for analyzing the model output. In Sect. 3, the results of the flux experiments are presented and discussed at multiple timescales. Section 4 summarizes the results and implications of this study.

2 Methods

In this study, we prescribe five global $FFCO_2$ emission fields that are introduced into the lowest atmospheric layer of a tracer transport model and subsequently run for four simulated years. Three years are considered a spin-up to allow $FFCO_2$ to reach equilibrium through the entire troposphere. The last year is used for analysis and the $FFCO_2$ mixing ratio is analyzed globally and at CO_2 observing sites.

2.1 $FFCO_2$ emissions

The $FFCO_2$ emissions data product, Fossil Fuel Data Assimilation System (FFDAS) version 2.0, is used as the flux boundary condition for the model simulations in this study (Asefi-Najafabady et al., 2014). The FFDAS $FFCO_2$ emissions were estimated using a diagnostic model (the Kaya identity), constrained by a series of spatially-explicit observational datasets, which decompose emissions into population, economics, energy, and carbon intensity terms (Rayner et al., 2010). The observational datasets used in the FFDAS include a remote sensing-based nighttime lights data product, the LandScan gridded population data product, national sector-based fossil fuel CO_2 emissions

ACPD
15, 20679–20708, 2015

from the International Energy Agency (IEA), and a recently-constructed database of global power plant CO_2 emissions (Elvidge et al., 2009; Asefi-Najafabady et al., 2014).

The FFDAS emissions are produced at $0.1^\circ \times 0.1^\circ$ resolution for the years 1997 to 2010. The emissions for year 2002 are used in this study. Sub-annual temporal structure is imposed on these annual emissions based on two additional datasets. Diurnal and weekly cycles are derived from a global data product (referred as TIMES hereafter) at $0.25^\circ \times 0.25^\circ$ resolution (Nassar et al., 2013). The monthly temporal cycle is obtained from the global data product developed by Andres et al. (2011) at a resolution of $0.1^\circ \times 0.1^\circ$ and similarly imposed on the FFDAS emissions. With these temporal structure datasets, five separate $FFCO_2$ emission fields are created:

1. A global $0.1^\circ \times 0.1^\circ$ $FFCO_2$ emission field in which only the diurnal cycle is represented ("diurnal cycle emissions"-DCE). This is accomplished by distributing the annual emission total in each grid cell evenly for every day of the year (divided by 365) and then distributing the daily total according to the hourly diurnal fractions from TIMES.

2. A global $0.1^\circ \times 0.1^\circ$ $FFCO_2$ emissions field in which only the weekly cycle is represented ("weekly cycle emissions"-WCE). This is accomplished by distributing the annual emissions in each grid cell evenly for each week of the year (divided by 52) and then distributing the weekly total according to the day-of-the-week fractions from TIMES.

3. A global $0.1^\circ \times 0.1^\circ$ $FFCO_2$ emission field in which only the monthly cycle is represented ("monthly cycle emissions"-MCE). This is accomplished by distributing the annual total $FFCO_2$ emissions in each grid cell according to the monthly fractions from Andres et al. (2011). To avoid discontinuity at the month boundaries, a cubic spline filter is applied.

4. A global $0.1^\circ \times 0.1^\circ$ $FFCO_2$ emission field that represents all of the sub-annual temporal structure ("all cycle emissions"-ACE). This is accomplished by applying

ACPD
15, 20679–20708, 2015

the MCE, WCE and DCE fractions in succession with the application of the cubic spline smoother and scaling to ensure conservation of mass.

5. A global 0.1° × 0.1v $FFCO_2$ emission field with no sub-annual temporal structure ("flat emissions"-FE). Hence, the annual amount in each grid cell is divided by 2920 to obtain evenly distributed emissions at three-hour model resolution.

To understand the temporal variations of the input $FFCO_2$ emission fields used in the simulations, we focus attention on areas of the planet with large $FFCO_2$ emissions, what we refer to as the "large source regions" (LSRs). These regions are located in the US (30 to 48° N, 125 to 70° W), Western Europe (40 to 60° N, 10° W to 40° E) and China (20to 45° N, 105 to 125° E).

The DCE $FFCO_2$ emissions over the three LSRs show a diurnal cycle (Fig. S1 in the Supplement) that is characterized by smaller emissions at night and in the early morning versus larger emissions starting at sunrise and remaining elevated until just after sunset. The DCE emissions typically reach a minimum value between midnight and 3:00 AM and a maximum value at ∼15:00 local time. This pattern is expected from the diurnal variations of human activity, such as waking versus sleeping hours and work-related activity cycles (e.g. on-road vehicle "rush" hours, starting and ending most daily work cycles). We also show the diurnal cycle of planetary boundary layer height used in this study (Fig. S1), which shows similar diurnal variation to the diurnal DCE $FFCO_2$ emissions.

The WCE $FFCO_2$ emissions reflect diminished economic activity on the weekends versus the weekdays. For most of the planet, Saturday and Sunday are the designated weekend days, but in some Middle Eastern countries, Thursday/Friday constitute the weekend days (Fig. S2).

The MCE $FFCO_2$ emissions reflect the different energy needs in winter versus summer: for example, due to space heating of buildings (Fig. S3). However, the space/time patterns reflect different fossil fuel-based energy use across the planet. For example, the $FFCO_2$ emissions in western Europe are larger in December and January and

ACPD
15, 20679–20708, 2015

smaller in July and August. The US also shows peak emissions in December–January, but with a second peak in July–August. The summer peak is due to electricity-driven air-conditioning prevalent in the United States (Gregg et al., 2009). China exhibits an unusual monthly variation, with the largest $FFCO_2$ emissions in December followed by a sudden drop in January and February, and then an increasing trend to December. This has been attributed to uncertainty in the underlying energy consumption data, discussed in detail in Gregg et al. (2008).

To enable atmospheric transport simulation, the five FFDAS emission fields were regridded from their original $0.1^\circ \times 0.1^\circ$ spatial resolution to the $1.25^\circ \times 1^\circ$ atmospheric transport model (see Sect. 2.3) resolution (longitude × latitude). When regridding, emissions originally emanating from land are often allocated to water-covered grid cells – an artifact typically encountered along coastlines when regridding from a fine to coarse resolution. Such a mismatch can lead to a dynamical inconsistency between the emissions and atmospheric transport. To avoid this error, we apply the "shuffling" reallocation method described in Zhang et al. (2014) for all five emissions fields. For the purposes of atmospheric transport simulations, the emissions derived from FFDAS for the year 2002 are repeated across all the years in the atmospheric transport model runs.

2.2 Biospheric fluxes

In order to place the impact of the temporal variation in $FFCO_2$ emissions within a larger context, an additional experiment is conducted driven by terrestrial biospheric carbon fluxes with diurnal and seasonal variations. The biospheric CO_2 flux is a recent version of that used in the TransCom experiment: CASA model NEE estimates with "neutral" annual fluxes (e.g. Peylin, 2014; Randerson et al., 1997) at a $1^\circ \times 1^\circ$ spatial resolution and three-hourly temporal resolution (referred as "CASA fluxes" hereafter). The terrestrial biospheric fluxes have a seasonal cycle, characterized by negative values (carbon uptake from the atmosphere to land) during the growing season (late spring and summer) versus positive fluxes (carbon release from the land to the atmosphere) during

ACPD
15, 20679–20708, 2015

the dormant season (winter and early spring) (Fig. S3). The biospheric fluxes also contain diurnal variation with typically negative values during the daytime (dominated by photosynthetic uptake) and positive values during the night (dominated by respiration) (Fig. S1)

The biospheric fluxes are regridded from the original 1° × 1° to the 1.25° × 1° transport model resolution with the same shuffling method used for the $FFCO_2$ emission fields.

2.3 Transport model

A global tracer transport model, the Parameterized Chemical Transport Model (PCTM), is used to simulate the $FFCO_2$ concentrations resulting from each of the five $FFCO_2$ emission fields (Kawa et al., 2004, 2010). The meteorological fields from the Goddard Earth Observing System Data Assimilation System Version 5 (GEOS-5) MERRA reanalysis products are used to drive the atmospheric transport (Reineker et al., 2008). The model uses a semi-Lagragian advection scheme (Lin and Rood, 1996); the subgrid-scale transport includes convection and boundary layer turbulence processes (McGrath-Spangler and Molod, 2014). The model grid is run at 1.25° longitude × 1° latitude with 72 hybrid vertical levels, and produces CO_2 concentration output every hour. The CO_2 concentration output from PCTM has been widely used in comparison with in situ and satellite measurements (Parazoo et al., 2012). It has been shown that PCTM simulates the diurnal, synoptic, and seasonal variability of CO_2 concentration well (e.g., Kawa et al., 2004, 2010; Law et al., 2008).

A total of six emission cases are run through the PCTM. The GEOS-5 meteorology has a 3 h time resolution and a 7.5 min time step is used in the model simulations.

2.4 Analysis methods

In this study, all five $FFCO_2$ simulations use the same meteorology and the same annual total $FFCO_2$ emissions. The only difference between the $FFCO_2$ simulations is the sub-annual temporal structure as described in Sect. 2.1. Hence, the resulting

ACPD
15, 20679–20708, 2015

atmospheric $FFCO_2$ concentration differences are due to the differences in the time structure of the $FFCO_2$ emissions only. The atmospheric $FFCO_2$ concentration is examined in two ways: (a) near the surface (at ∼998 hPa; in the bottom layer which is ∼126 m or ∼15 hPa thick) and (b) as a pressure-weighted column integral. In order to understand how the different cyclic components of the $FFCO_2$ emissions interact with the simulated atmospheric transport at multiple time scales, we present the simulated $FFCO_2$ concentration results for the annual mean, and individual sub-annual cycles for both near-surface and column-integral (diurnal, weekly, monthly). In addition to global difference maps, concentration differences between the cyclic and flat $FFCO_2$ emissions are examined at selected GLOBALVIEW-CO_2 monitoring sites (http://www.esrl.noaa.gov/gmd/ccgg/globalview/co2/) (Masarie and Tans, 1995).

The impact of the $FFCO_2$ emissions' sub-annual temporal structure is defined as the simulated concentration difference between each sub-annually varying $FFCO_2$ emission field and the FE emission field, when averaged over specific time-cycles:

$$\Delta C_{it} = \frac{1}{N}\sum_{k=1}^{N}\left(\frac{1}{M}\sum_{j=1}^{M}C_{it(j,k)} - \frac{1}{M}\sum_{j=1}^{M}C_{if(j,k)}\right) \quad (1)$$

where ΔC_{it} is the mean concentration difference at the ith grid cell for cyclic emissions, N is the total counts of cycles over the investigated period, $C_{it(j,k)}$ is the jth hourly concentration in the kth cycle at the ith grid cell for cyclic emissions, M is the total counts of hourly periods for each cyclic emissions, $C_{if(j,k)}$ is the jth hourly concentration in the kth cycle at the ith grid cell for flat emissions.

By utilizing Eq. (1), the impact on simulated CO_2 concentration is examined for each individual sub-annual $FFCO_2$ emissions cycle and their combination. Impacts include:

1. the annual mean full-day concentration difference between each cyclic $FFCO_2$ emission and the flat emission fields, in order to explore $FFCO_2$ emissions rectification;

ACPD
15, 20679–20708, 2015

2. the annual mean afternoon (noon to 6 pm local time) concentration difference between the DCE and FE emission fields, to examine the impact at typical atmospheric monitoring times;

3. the annual daily mean concentration difference on weekdays/weekends between the WCE and FE emission fields, to examine the impact of weekly cycles;

4. the diurnal amplitude of hourly mean concentration difference over the year between the DCE and FE emission fields, to examine the impact of diurnal cycles, and

5. the seasonal amplitude of monthly mean concentration difference between MCE and FE emission fields, to examine the impact of the seasonal cycles.

The amplitude of the simulated concentration differences for DCE and the MCE simulations is defined as:

$$C_{\text{amp},\,it} = C_{\max,it}\left\{\Delta C_{itj}|_{j=1,\,M}\right\} - C_{\min,it}\left\{\Delta C_{itj}|_{j=1,M}\right\} \quad (2)$$

where $C_{\text{amp},\,it}$ is the amplitude at the ith grid cell, $C_{\max,it}$ is the maximum of the concentration differences at the ith grid cell, $C_{\min,it}$ is the minimum of the concentration differences at the ith grid cell, and ΔC_{itj} is the mean concentration difference for the jth point of the sub-annual cycle at the ith grid cell that is defined as Eq. (1), M is the total points of the sub-annual cycle.

3 Results and discussion

3.1 The $FFCO_2$ rectifier

Figure 1a shows the annual mean full-day surface $FFCO_2$ concentration difference between the ACE and FE emission fields (ACE minus FE). Despite the same annually integrated emissions at each grid cell, the annual mean surface concentration difference

ACPD
15, 20679–20708, 2015

shows non-zero values, suggesting rectification of the $FFCO_2$ emissions. The largest negative surface $FFCO_2$ concentration differences (up to −1.35 ppm) are found over the LSRs, coincident with the largest fossil fuel-based industrial activity and energy consumption. Smaller positive surface $FFCO_2$ concentration differences (up to 0.13 ppm) appear over north and northeastern Europe and western Siberia. The annual mean surface $FFCO_2$ concentration difference between the DCE and FE and the MCE and FE are shown in Fig. 1b and c, respectively. The negative surface $FFCO_2$ concentration differences in Fig. 1a are primarily driven by the DCE emissions (Fig. 1b) while the positive differences are primarily driven by the MCE emissions (Fig. 1c). Figure 1a includes the contribution from the WCE emissions, but no rectification results from this emission cycle at annual scales (Fig. S4).

Over the LSRs, the diurnal $FFCO_2$ emissions are temporally correlated with the diurnal variation of the PBL (Fig. S1). The emissions are largest during daytime when the PBL is well-mixed, so air with enriched CO_2 tends to be transported aloft. By contrast, the smaller nighttime $FFCO_2$ emissions are mixed into a typically shallower and stable PBL, so this lower-CO_2 air is confined closer to the surface. This covariation, when compared to the same dynamic coupling in the FE field, leads to greater $FFCO_2$ loss from the surface to the free troposphere in the ACE simulation, resulting in the negative annual mean surface $FFCO_2$ concentration difference values over the LSRs. The negative DCE rectification is up to −1.44 ppm at the grid cell scale over the western US (Fig. 1b). Note that the diurnal $FFCO_2$ rectifier effect shows little variation across the LSRs, due mainly to the similar diurnal amplitude of the diurnal emission fields.

The annual mean surface $FFCO_2$ concentration differences between the MCE and flat FE emissions are largest over the LSRs during the local winter months and smallest during the local summer months (Fig. S3). This variation interacts with simultaneous variations in PBL variation. However, distinct from the diurnal $FFCO_2$ rectification, the seasonal $FFCO_2$ rectification shows positive values (up to 0.23 ppm) for north-and-northeastern Europe versus negative values (up to −0.28 ppm) in East Asia, and a near-zero signal (no rectification) in the US (Fig. 1c). The positive rectification obtained

ACPD
15, 20679–20708, 2015

in north-and-northeastern Europe to Siberia is associated with the coincidence of large wintertime $FFCO_2$ emissions and weak wintertime atmospheric mixing, which tends to trap CO_2-enriched air near the surface. Additionally, the greater vertical mixing in summertime interacts with the smaller summer $FFCO_2$ emissions, thus, distributing more of the CO_2-depleted air to the free troposphere. The limited seasonal rectification in North America versus the other LSRs is mainly due to the more complex $FFCO_2$ emissions seasonality, with peak emissions in both the winter and summer months as shown previously. Finally, the negative rectification in East Asia is mainly ascribed to the previously mentioned anomalous monthly $FFCO_2$ emissions in China (increasing trend from January to December) and their interaction with atmospheric transport. Hence, the CO_2-depleted air is confined to the surface in East Asia by the very small $FFCO_2$ emissions combined with the inactive atmospheric transport in January and February.

The rectification of the $FFCO_2$ fluxes can be compared to the well-known biosphere flux rectifier. Surface concentration differences of up to 20.35 ppm at the grid cell scale for the biospheric flux simulation (Fig. S5) are centered over the tropical land and northern mid-to-high latitudes with much greater spatial extent than found for either the diurnal or seasonal $FFCO_2$ rectifier. Similar to the $FFCO_2$ rectification, the biospheric rectifier is a combination of diurnal and seasonal rectifications (e.g., Denning et al., 1995, 1996; Yi et al., 2004; Chen et al., 2004; Chan et al., 2008; Williams et al., 2011). For the diurnal biospheric rectification, the daytime net negative CASA fluxes typically coincide with a well-mixed PBL and greater interaction with the free troposphere. At night, this flux is typically reversed and mixed into a shallow PBL, resulting in a positive full-day annual mean surface CO_2 concentration due to the greater loss of CO_2-depleted air during the day. In the case of the seasonal biospheric rectifier, the summer net negative CASA fluxes are mixed into a thicker PBL, resulting in a strong negative surface perturbation, whereas the winter net positive CASA fluxes are mixed into a thinner PBL, resulting in a weaker positive perturbation. The two interactions combine to give a positive annual mean surface CO_2 concentration. The above analysis indicates that $FFCO_2$ rectification is mechanistically similar to biospheric rectification, but the $FFCO_2$

ACPD
15, 20679–20708, 2015

rectifier effect occurs mainly at local-to-regional scales while the biosphere rectification is expressed at a larger spatial scale.

3.2 Impact on afternoon sampling

Atmospheric inversion studies of CO_2 fluxes using flask and tall tower atmospheric CO_2 measurements require consideration of CO_2 concentration sampling times (e.g. Peters et al., 2007; Dang et al., 2011). Given the importance of the simulated CO_2 concentration to the diurnal cycle of $FFCO_2$ emissions, we sub-sample the DCE $FFCO_2$ simulation output for local afternoon (noon–18:00 p.m.) conditions. Figure 2 presents the spatial distribution of the annual mean, afternoon-only surface $FFCO_2$ concentration difference between the DCE and FE fields. Values vary from −0.21 to +1.13 ppm, with larger positive values centered over the LSRs. Negative values are mainly due to the interaction of small emissions and a stable PBL at nighttime and the early morning. The afternoon and 24 h mean signals (Fig. 1b) are of opposite signs but roughly the same magnitude over the LSRs. This is due to the afternoon signal being sampled at the time of the largest afternoon emissions, but also contributing the weakest surface signal to the 24 h diurnal span. The afternoon mean signal indicates that a potential bias would be incurred by ignoring the diurnal variability of the $FFCO_2$ emissions. It is noteworthy that the afternoon effect mainly occurs at the local scale, and has a much smaller spatial extent than the full-day diurnal rectification. This indicates that CO_2 monitoring strategies could minimize the effect of the $FFCO_2$ diurnal cycle when using afternoon measurements and the measurements can be taken close to large source regions for studies influenced by the diurnal cycle.

3.3 Impact of the diurnal amplitude

The continuous atmospheric CO_2 measurements taken by many monitoring stations can see the complete 24 h coverage of atmospheric CO_2 concentration, and can enable the estimate of sub-daily fluxes in inversion studies using these data (e.g., Law et al.,

ACPD
15, 20679–20708, 2015

2008). This motivates the examination of the diurnal peak-to-peak amplitude of the simulated concentration, since this parameter includes the overall daily information of the diurnal $FFCO_2$ concentration.

Figure 3a displays the amplitude of the annual mean diurnal surface concentration difference between the DCE and FE fields across the globe. The largest amplitude values are centered over the LSRs with peak-to-peak values reaching 9.12 ppm in western US (−117° E, 34° N). Local sunrise is the point when the $FFCO_2$ concentrations reach their greatest difference. At local sunrise, the FE emissions exceed the DCE emissions, which are small prior to the increase of daytime emitting activity (Fig. S1). When combined with the minimum in vertical mixing and a shallow nighttime PBL, the resulting $FFCO_2$ concentration difference is negative (DCE minus FE). Local sunset, by contrast, is the point in the annual mean diurnal cycle where the differences between the DCE and FE fields are at their smallest (Fig. S1) and the DCE emissions exceed those of FE. This combines with the much greater vertical mixing and greater PBL height, and tends to ameliorate the resulting surface $FFCO_2$ concentration difference. Hence, the amplitude difference is driven primarily by the concentration difference at the minima of the diurnal cycle (local sunrise).

To provide context for the magnitude of the $FFCO_2$ diurnal amplitude, the surface $FFCO_2$ DCE concentration amplitude can be compared to that resulting from biosphere fluxes. This is shown in Fig. 3b, where the ratio of $FFCO_2$ amplitude to the total of the $FFCO_2$ and biosphere amplitudes is presented. Averaged over the LSRs, the diurnal amplitude of the annual mean $FFCO_2$ concentration accounts for more than 15 % of the total diurnal amplitude, and this ratio rises as high as 87 % at the grid cell scale over the LSRs (corresponding to a $FFCO_2$ diurnal amplitude that is 5 ppm larger than the biospheric amplitude, Fig. 3b). The diurnal amplitude can be examined seasonally as well. The diurnal $FFCO_2$ amplitude accounts for a larger portion (up to 5 ppm) of the total diurnal variation than the diurnal biospheric amplitude in winter when the biosphere is relatively quiescent and vertical mixing is less vigorous (Fig. S6). Overall, this result

ACPD
15, 20679–20708, 2015

indicates that studies of diurnal atmospheric CO_2 should consider the contribution of diurnal $FFCO_2$ emissions, especially over LSRs and in wintertime.

3.4 Impact of the seasonal amplitude

Figure 4 shows the amplitude of monthly CO_2 concentration difference between the MCE and FE (MCE- FE) fluxes. The seasonal amplitude varies from 0.01 to 6.11 ppm, with large signals over the LSRs as seen in previous figures. Both the magnitude and spatial extent are larger than found in the diurnal case. The longer periodicity allows more time for an atmospheric signal to build up and to be advected further from the emission source regions. The seasonal maxima and minima contribute equally to the amplitude for all regions (Fig. S7). The seasonal maximum mainly occurs in December–January, driven by the larger $FFCO_2$ emissions during winter (Fig. S8). The seasonal minimum exhibits variable timing across the LSRs, with January for China (up to −3.42 ppm), August/September for the US (−1.09 ppm) and June/July for west Europe (−2.55 ppm). This timing is consistent with the timing of the smallest $FFCO_2$ emissions over each region (Fig. S8). The seasonal minimum in East Asia is, as has been mentioned, likely an artifact of the inventory statistics.

The $FFCO_2$ seasonal amplitude can also be compared to the seasonal biospheric amplitude, for context (Fig. 4b). The biospheric amplitudes are much larger than the $FFCO_2$ amplitudes at the global scale, except for specific industrialized source regions in the US, western Europe and East Asia, where the $FFCO_2$ amplitude accounts for more than 25 % of the total seasonal amplitude. This result indicates a non-negligible local-to-regional $FFCO_2$ effect on seasonal amplitude of atmospheric CO_2 concentration.

3.5 Impact of the weekly cycle

The impact of the weekly cycle of $FFCO_2$ emissions is demonstrated here by constructing a mean weekday and mean weekend surface $FFCO_2$ concentration from the

ACPD
15, 20679–20708, 2015

difference between the WCE and FE simulations (Fig. 5). As expected, the surface $FFCO_2$ difference values are centered over LSRs, with predominantly positive $FFCO_2$ concentration values for the weekdays and negative values on the weekends. The negative weekend values are a reflection of the reduced weekend $FFCO_2$ emissions versus weekday activity (Nassar et al., 2013). There are a few deviations from this regular weekday/weekend pattern. First, the different definition of what constitutes weekend activity is seen over the Middle East, where the weekend is typically Thursday–Friday versus Saturday–Sunday in most of the rest of the world. In contrast to other weekdays, Monday shows positive values only in narrow portions of East Asia. The other large source regions show negative surface $FFCO_2$ concentration difference values. This spatial pattern results from the downwind transport of the lower weekend $FFCO_2$ emissions. This coherent $FFCO_2$ concentration difference dissipates after 24 h and is then dominated by the higher weekday $FFCO_2$ emissions. The downwind transport of the larger Friday $FFCO_2$ emissions isn't shown clearly on the simulated weekend $FFCO_2$ concentration, due mainly to the dominant effect of the lower weekend emissions.

3.6 Sampling at monitoring stations

Atmospheric CO_2 monitoring locations were originally sited away from fossil fuel source regions, but as $FFCO_2$ emissions have risen dramatically over time, they are increasingly influenced by $FFCO_2$ sources. A large number of monitoring stations are situated in strongly affected areas in temperate North America, Western Europe and East Asia that show a strong diurnal concentration. Noteworthy are the coastal sites close to the large source regions in the US and Western Europe – these show significant influence from the DCE flux component, despite the fact that these locations are assumed to represent upwind background CO_2. Timeseries of daily afternoon-mean CO_2 concentration differences demonstrate this influence (Fig. 6). For the sake of brevity, we focus on two stations: La Jolla, in the western US (32.9° N, 117.3° W, 10 m, referred as LJO) and Lutjewad of the Netherlands (53.4° N, 6.35° E, 61 m, referred as LUTDTA). The two

ACPD
15, 20679–20708, 2015

sites were selected because they are close to LSRs (locations highlighted in the figure). A strong seasonality of up to 5 ppm for LUTDTA and up to 3 ppm for LJO is shown in the daily afternoon mean CO_2 concentration difference from the ACE simulation. Synoptic variability with approximately the same magnitude is also evident (Fig. 6b). Finally, a slight weekly cycle can be seen in spring and summer at both stations.

The timeseries can be further understood through examination of the cyclic $FFCO_2$ flux contributions (Fig. 6c–e). The MCE simulation shows the largest daily afternoon mean impact on CO_2 concentrations (up to 5.5 ppm) versus smaller values for the WCE (2.2 ppm) and DCE (1.6 ppm). Large seasonality is shown in the MCE that is caused by the interaction of the monthly $FFCO_2$ emissions and atmospheric transport. The WCE and DCE display slight but evident seasonality that is driven mainly by the seasonal atmospheric transport. Synoptic variability is seen in the MCE (up to 4 ppm) and DCE (up to 1 ppm). Also, a weekly cycle is illustrated for the WCE driven by the weekly $FFCO_2$ emissions. These temporal patterns are common to the stations with significant response to the time-cycle $FFCO_2$ emissions, but the magnitude is dependent on the local dynamical conditions, transport patterns and proximity of the site to the $FFCO_2$ sources. LJO shows a larger impact than LUTDTA in July and August, associated mainly with the large $FFCO_2$ emissions in summer. Differences are found in the timing of the synoptic events between the two sites, and the amplitude of the synoptic variation in the CO_2 concentration difference at LUTDTA is roughly twice that at LJO, which suggests that the synoptic events of atmospheric transport play an important role in distributing the $FFCO_2$ at LUTDTA.

3.7 Column-average concentration

The analysis above indicates significant CO_2 concentration response to sub-annual $FFCO_2$ emission variability near the surface. With the advent of satellite measurements, as well as the surface-based spectrometers of the TCCON network, it is important to examine the response of vertically-average CO_2 concentrations to the $FFCO_2$ emissions. How important is sub-annual $FFCO_2$ emission variability to the CO_2 con-

ACPD
15, 20679–20708, 2015

centration seen from space? And what impact do these $FFCO_2$ emission cycles have on studies that use satellite measurements?

To answer these questions, the same analysis is performed for the simulated column-integral CO_2 concentration for all the cyclic $FFCO_2$ emissions as was performed for the surface. For generality, we have used straight pressure weighting to compute the column averages, rather than use the vertical weighting appropriate for any particular satellite. Results indicate weak rectifier effects in the simulated column-integral $FFCO_2$ concentration, with ACE having negative values from −0.02 to −0.06 ppm. The ACE rectification is centered over large source regions and the MCE component represents the largest contribution overall; varying from −0.02 to −0.06 ppm (Fig. S9). The DCE exhibits similar rectification magnitudes varying from −0.02 to −0.04 ppm, but with a response covering a smaller spatial extent. The MCE rectification reflects the larger vertical and spatial effect of the monthly $FFCO_2$ emission variability as compared to the WCE and DCE. Compared to the surface effect, the column-integral rectification is almost an order of magnitude smaller. However, note the negative signal in west Europe from MCE, which is opposite to the positive signal at the surface (Fig. 1). Overall, the sub-annual $FFCO_2$ emission variability has little effect on all aspects of the column-integral CO_2 concentration.

4 Conclusions and implication

This study investigates the impact of sub-annual $FFCO_2$ emissions cycles (diurnal, weekly and monthly) on the simulated CO_2 concentration. The simulated CO_2 concentrations are examined at multiple time scales over the globe as well as at GlobalView monitoring stations. When expressed as annual means, a $FFCO_2$ rectifier effect is found from the combination of all cycles, which varies from −1.35 to +0.13 ppm, centered over large source regions in the northern hemisphere. This is driven by a large negative diurnal $FFCO_2$ rectification due to the interaction of large/smaller $FFCO_2$ emissions with vigorous/inactive PBL mixing in the daytime/nighttime, and a positive

ACPD
15, 20679–20708, 2015

seasonal rectification in Western Europe resulting from the covariance of small/larger $FFCO_2$ emissions in the summertime/wintertime with vigorous/inactive atmospheric transport.

The diurnal $FFCO_2$ emissions are also found to significantly affect the diurnal variation of simulated CO_2 concentrations at the local/regional scale, driven by the covariance of diurnally-varying $FFCO_2$ emissions and vertical mixing. The impact on the diurnal peak-to-peak amplitude is up to 9.12 ppm while the impact on the afternoon mean concentration is as large as +1.13 ppm at the grid cell scale. The results indicate the importance of proper temporal sampling when using/interpreting measurements affected by diurnal $FFCO_2$ emissions (especially those near emission regions). The small spatial extent of the afternoon effect suggests that measurements can be taken close to the large source regions when required for studies that use the afternoon-only measurements.

The monthly $FFCO_2$ variability results in a simulated CO_2 concentration seasonal amplitude (up to 6.11 ppm) over large source regions, caused mainly by the interaction of large/smaller $FFCO_2$ emissions in wintertime/summertime with inactive/vigorous PBL mixing. Significant spatial patterns are found at the regional scale, due mainly to the large difference in the seasonal variations of $FFCO_2$ emissions across the regions. This result suggests that attention should be given to accurate representation of seasonal profiles of regional emission inventories, particularly for large emitters like China. The diurnal response has a more limited spatial extent than the monthly response and can probably be disregarded when considering clean air oceanic sites.

The simulated CO_2 concentration at the GlobalView stations are found to be affected by all sub-annual $FFCO_2$ cycles, especially for sites close to large source regions. These impacts cover multiple time-scales, from diurnal to seasonal, caused by the interaction/combination of the variable $FFCO_2$ emissions with atmospheric transport. This finding, together with the above, indicates that current inversion studies that do not incorporate sub-annually varying $FFCO_2$ emissions could result in biased flux estimates results due to the $FFCO_2$ rectifier, and that caution should be taken regard-

ACPD
15, 20679–20708, 2015

ing sampling time and when choosing the locations for new sites of atmospheric CO_2 measurement.

Characterization of the column-average simulated CO_2 concentration suggests a weak impact compared to the surface signal, indicating less importance than for surface measurements. This also suggests that including the sub-annual cycles of $FFCO_2$ variability is not as important a concern for modeling studies using only satellite measurements.

The Supplement related to this article is available online at doi:10.5194/acpd-15-20679-2015-supplement.

Acknowledgements. This work was supported by the National Science Foundation CAREER award 0846358 and NASA ROSES grant NNX11AH86G. P. Rayner is supported by an Australian Professorial Fellowship (DP1096309).

References

Andres, R. J., Gregg, J. S., Losey, L., Marland, G., and Boden, T. A.: Monthly, global emissions of carbon dioxide from fossil fuel consumption, Tellus, 63B, 309–327, 2011.

Asefi-Najafabady, S., Rayner, S. P. J., Gurney, K. R., McRobert, K. R. A., Song, Y., Coltin, K., Huang, J., Elvidge, C., and Baugh, K.: A multiyear, global gridded fossil fuel CO_2 emissions data product: Evaluation and analysis of results, J. Geophys. Res. Atmos., 119, 10213–10231, doi:10.1002/2013JD021296, 2014.

Chan, D., Ishizawa, M., Higuchi, K., Maksyutov, S., and Chen, J.: Seasonal CO_2 rectifier effect and large-scale extratropical atmospheric transport, J. Geophys. Res. Atmos, 113, D17309, doi:10.1029/2007JD009443, 2008.

Chen, B. and Chen, J. M.: A vertical diffusion scheme to estimate the atmospheric rectifier effect, J. Geophys. Res., 109, D04306, doi:10.1029/2003JD003925, 2004.

Ciais, P., J., Paris, D., Marland, G., Peylin, P., Piao, S. L., Levin, I., Pregger, T., Scholz, Y., Friedrich, R., Rivier, L., Houwelling, S., Schulze, E. D., and members of the CARBOEUROPE

ACPD
15, 20679–20708, 2015

Synthesis Team (1): The European carbon balance revisited. Part 1: fossil fuel emissions, Global Change Biol., 16, 1395–1408, doi:10.1111/j.1365-2486.2009.02098.x, 2009.
Dang, X., Lai, C.-T., Hollinger, D. Y., Schauer, A. J., Xiao, J., Munger, J. W., Owensby, C., and Ehleringer, J. R.: Combining tower mixing ratio and community model data to estimate regional-scale net ecosystem carbon exchange by boundary layer inversion over four flux twoers in the United States, J. Geophys. Res., 116, G03036, doi:10.1029/2010JG001554, 2011.
Denning, A. S., Fung, I. Y., and Randall, D. A.: Lantitudinal gradient of atmospheric CO_2 due to seasonal exchange with land biota, Nature, 376, 240–243, 1995.
Denning, A. S., Collatz, G. J., Zhang, C., Randall, D. A., Berry, J. A., Sellers, P. J., Colello, G. D., and Dazlich, D. A.: Simulations of terrestrial carbon metabolism and atmospheric CO_2 in a general circulation model. Part 2: simulated CO_2 concentrations, Tellus, 48B, 543–567, 1996.
Elvidge, C. D., Ziskin, D., Baugh, K. E., Tuttle, B. T., Ghosh, T., Pack, D. W., Erwin, E. H., and Zhizhin, M.:, A Fifteen Year Record of Global Natural Gas Flaring Derived from Satellite Data, Energies, 2, 595–622, 2009.
Enting, I.: Inverse Problems in Atmospheric Constituent Transport, Cambridge Univ. Press, New York, 2002.
Field, C. B., Lobell, D. B., Peters, H. A., and Chiariello, N. R.: Feedbacks of terrestrial ecosystems to climate change, Annu. Rev. Environ. Resour., 32, 1–29, doi:10.1146/annurev.energy.32.053006.141119, 2007.
Gregg, J. S., Andres, R. J., and Marland, G.: China: emissions pattern of the world leader in CO_2 emissions from fossil fuel consumption and cement production. Geophys. Res. Lett., 35, L08806, doi:10.1029/2007GL032887, 2008.
Gregg, J. S., Losey, L. M., Andres, R. J., Blasing, G. J., and Marland, G.: The temporal and spatial distribution of carbon dioxide emissions from fossil-fuel use in North America, J. Appl. Meteorol. Climatol., 48, 2528–2542, doi:10.1175/2009JAMC2115.1, 2009.
Gurney, K. R., Law, R. M., Denning, A. S., Rayner, P. J., Baker, D., Bousquet, P., Bruhwiler, L., Chen, Y.-H., Ciais, P., Fan, S., Fung, I. Y., Gloor, M., Heimann, M., Higuchi, K., John, J., Maki, T., Maksyutov, S., Masarie, K., Peylin, P., Prather, M., Pak, B. C., Randerson, J., Sarmiento, J., Taguchi, S., Takahashi, T., and Yuen, C.-W.: Towards robust regional estimates of CO_2 sources and sinks using atmospheric transport models, Nature, 415, 626–630, 2002.

ACPD
15, 20679–20708, 2015

Gurney, K. R., Chen, Y., Maki, T., Kawa, S. R., Andrews, A., and Zhu, Z.: Sensitivity of atmospheric CO_2 inversions to seasonal and interannual variations in fossil fuel emissions, J. Geophys. Res., 110, D10308, doi:10.1029/2004JD005373, 2005.

Kawa, S. R., Erickson III, D. J., Pawson, S., and Zhu, Z.: Global CO_2 transport simulations using meteorological data from the NASA data assimilation system, J. Geophys. Res., 109, D18312, doi:10.1029/2004JD004554, 2004.

Kawa, S. R., Mao, J., Abshire, J. B., Collatz, G., and Weaver, C. J.: Simulation studies for a space-based CO_2 lidar mission, Tellus, 62B, 759–769, 2010.

Keeling, C. D., Bacastow, R. B., Carter, A. F., Piper, S. C., Whorf, T. P., Heimann, M., Mook, W. G., and Roeloffzen, H.: A three-dimensional model of atmospheric CO_2 trasport based on observed winds. 1: Analysis of observed data, in: Aspects of Climate Variability in the Pacific and Western Americas, Geophys. Monogr. Ser., vol. 55, edited by: Peterson, D. H., 165–236, AGU, Washington, DC, 1989.

Law, R. M., Peters, W., Rödenbeck, C., Aulagnier, C., Baker, I., Bergmann, D. J., Bousquet, P., Brandt, J., Bruhwiler, L., Cameron-Smith, P. J., Christensen, J. H., Delage, F., Denning, A. S., Fan, S., Geels, C., Houweling, S., Imasu, R., Karstens, U., Kawa, S. R., Kleist, J., Krol, M. C., Lin, S.-J., Lokupitiya, R., Maki, T., Maksyutov, S., Niwa, Y., Onishi, R., Parazoo, N., Patra, P. K., Pieterse, G., Rivier, L., Satoh, M., Serrar, S., Taguchi, S., Takigawa, M., Vautard, R., Vermeulen, A. T., and Zhu, Z.: : TransCom model simulations of hourly atmospheric CO_2: Experimental overview and diurnal cycle results for 2002, Global Biogeochem. Cy., 22, GB3009, doi:10.1029/2007GB003050, 2008.

Masarie, K. A. and Tans, P. P.: Extension and Integration of Atmospheric Carbon Dioxide Data into a Globally Consistent Measurement Record. J. Geophys. Res., 100, 11593–11610, 1995.

McGrath-Spangler, E. L. and Molod, A.: Comparison of GEOS-5 AGCM planetary boundary layer depths computed with various definitions, Atmos. Chem. Phys., 14, 6717–6727, doi:10.5194/acp-14-6717-2014, 2014.

Nassar, R., Napier-Linton, L., Gurney, K. R., Andres, R. J., Oda, T., Vogel, F. R., and Deng, F.: Improving the temporal and spatial distribution of CO_2 emissions from global fossil fuel emission data sets, J. Geophys. Res. Atmos., 118, 917–933, 2013.

Parazoo, N. C., Denning, A. S., Kawa, S. R., Pawson, S., and Lokupitiya, R.: CO_2 flux estimation errors associated with moist atmospheric processes, Atmos. Chem. Phys., 12, 6405–6416, doi:10.5194/acp-12-6405-2012, 2012.

ACPD
15, 20679–20708, 2015

Peters, W., Jacobson, A. R., Sweeney, C., Andrews, A. E., Conway, T. J., Masarle, K., Miller, J. B., Bruhwiler, L. M. P., Pètron, G., Hirsch, A. I., Worthy, D. E. J., vander Werf, G. R., Randerson, J. T., Wennberg, P. O., Krol, M. C., and Tans, P. P.: An atmospheric perspective on North American carbon dioxide exchange: CarbonTracker, Proc. Natl. Aca. Sci., 104, 18925–18930, 2007.

Peylin, P., Houweling, S., Krol, M. C., Karstens, U., Rödenbeck, C., Geels, C., Vermeulen, A., Badawy, B., Aulagnier, C., Pregger, T., Delage, F., Pieterse, G., Ciais, P., and Heimann, M.: Importance of fossil fuel emission uncertainties over Europe for CO_2 modeling: model intercomparison, Atmos. Chem. Phys., 11, 6607–6622, doi:10.5194/acp-11-6607-2011, 2011.

Peylin, P., Law, R. M., Gurney, K. R., Chevallier, F., Jacobson, A. R., Maki, T., Niwa, Y., Patra, P. K., Peters, W., Rayner, P. J., Rödenbeck, C., van der Laan-Luijkx, I. T., and Zhang, X.: Global atmospheric carbon budget: results from an ensemble of atmospheric CO_2 inversions, Biogeosciences, 10, 6699–6720, doi:10.5194/bg-10-6699-2013, 2013.

Rayner, P. J., Raupach, M. R., Paget, M., Peylin, P., and Koffi, E.: A new global gridded data set of CO_2 emissions from fossil fuel combustion: Methodology and evaluation, J. Geophys. Res., 115, D19306, doi:10.1029/2009JD013439, 2010.

Reineker, M. M., Suarez, M. J., Todling, R., Bacmeister, J., Takacs, L., Liu, H.-C., Gu, W., Sienkiewicz, M., Koster, R. D., Gelaro, R., Stajner, I., and Nielsen, J. E.: The GEOS-5 Data Assimilation System – Documentation of Versions 5.0.1, 5.1.0, and 5.2.0, NASA Technical Report Series on Global Modeling and Data Assimilation, V27, 2008.

Tans, P. P., Fung, I. Y.., and Takahashi, T.: Observational constraints on the global atmospheric CO_2 budget, Science, 247, 1431–1438, 1990.

Williams, I. N., Riley, W. J., Torn, M. S., Berry, J. A., and Biraud, S. C.: Using boundary layer equilibrium to reduce uncertainties in transport models and CO_2 flux inversions, Atmos. Chem. Phys., 11, 9631–9641, doi:10.5194/acp-11-9631-2011, 2011.

Yi, C., Davis, K. J., Bakwin, P. S., Denning, A. S., Zhang, N., Desai, A., Lin, J. C., and Gerbig, C.: Observed covariance between ecosystem carbon exchange and atmospheric boundary layer dynamics at a site in northern Wisconsin, J. Geophys. Res., 109, D08302, doi:10.1029/2003JD004164, 2004.

Zhang, X., Gurney, K. R., Rayner, P., Liu, Y., and Asefi-Najafabady, S.: Sensitivity of simulated CO_2 concentration to regridding of global fossil fuel CO_2 emissions, Geosci. Model Dev., 7, 2867–2874, doi:10.5194/gmd-7-2867-2014, 2014.

ACPD
15, 20679–20708, 2015

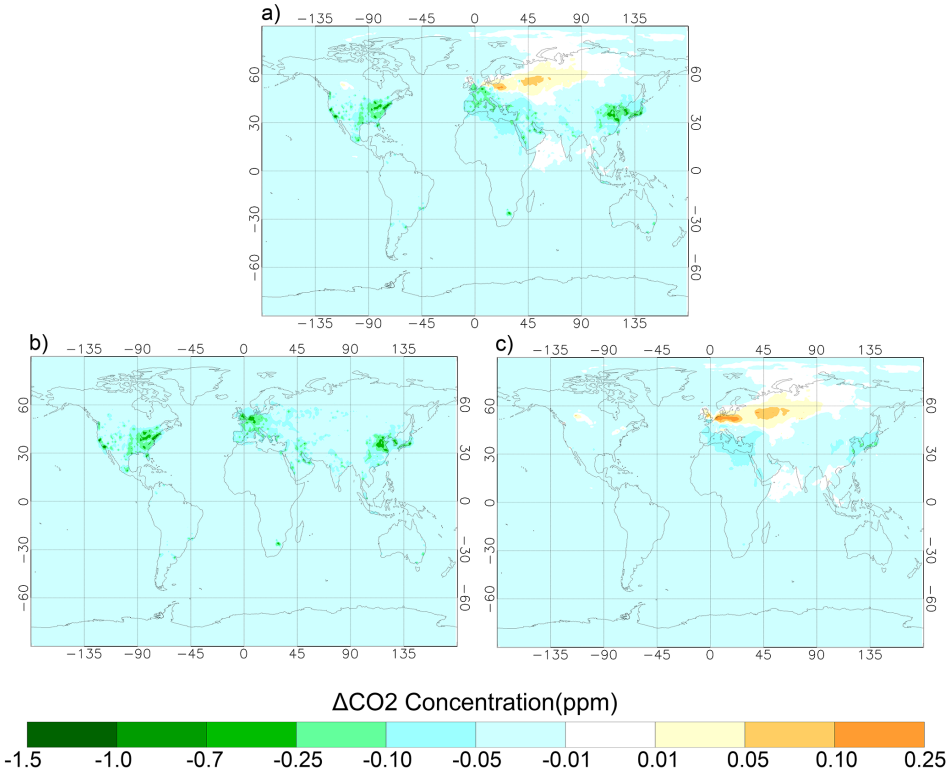

Figure 1. Simulated full-day annual mean surface $FFCO_2$ concentration difference between the time-varying and flat $FFCO_2$ emission fields. **(a)** ACE minus FE; **(b)** DCE minus FE; **(c)** MCE minus FE.

ACPD
15, 20679–20708, 2015

Sensitivity of simulated CO_2 concentration to sub-annual variations

X. Zhang et al.

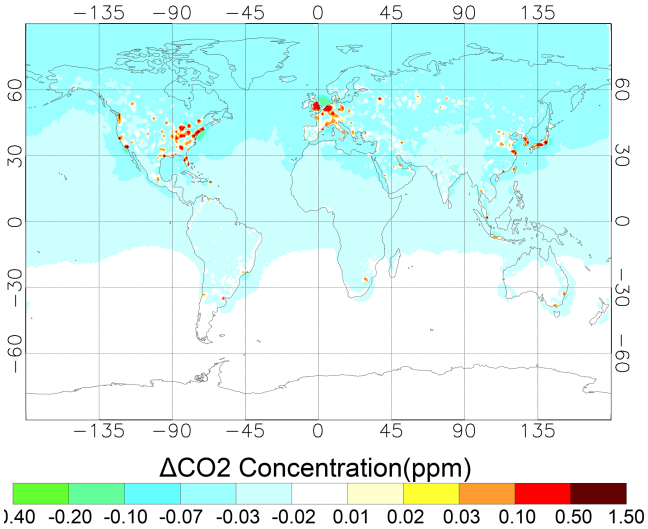

Figure 2. Simulated annual mean surface $FFCO_2$ concentration difference between the DCE and FE $FFCO_2$ emission fields (DCE minus FE), sampled during the local afternoon (12:00–18:00).

ACPD
15, 20679–20708, 2015

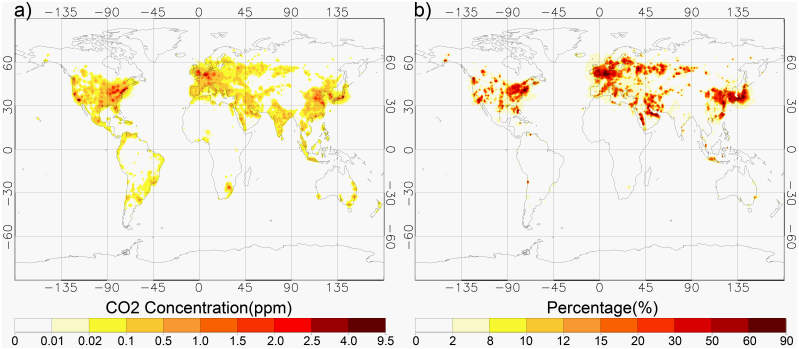

Figure 3. The diurnal amplitude of the $FFCO_2$ surface concentration from the DCE simulation. **(a)** the peak-to-peak diurnal amplitude of the annual mean, hourly concentration difference between the DCE and FE emission fields (DCE minus FE); **(b)** ratio of $FFCO_2$ diurnal amplitude to the diurnal CO_2 amplitude of total $FFCO_2$ and biosphere.

ACPD
15, 20679–20708, 2015

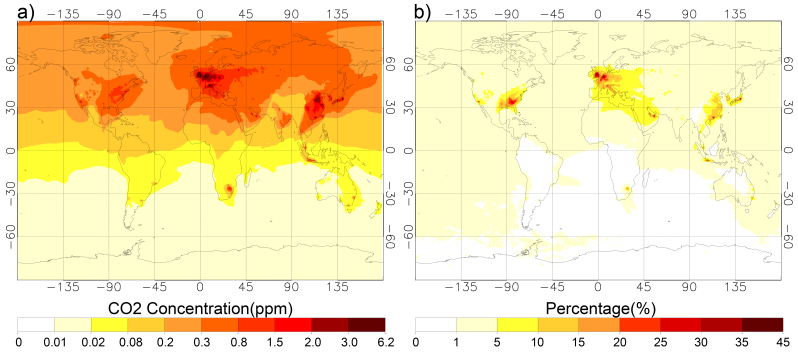

Figure 4. Seasonal amplitude of the simulated surface $FFCO_2$ concentration; **(a)** peak-to-peak seasonal amplitude of simulated surface $FFCO_2$ concentration difference between the MCE and FE emission fields (MCE minus FE); **(b)** ratio of $FFCO_2$ seasonal amplitude to the sum of the $FFCO_2$ and biosphere seasonal amplitude.

ACPD
15, 20679–20708, 2015

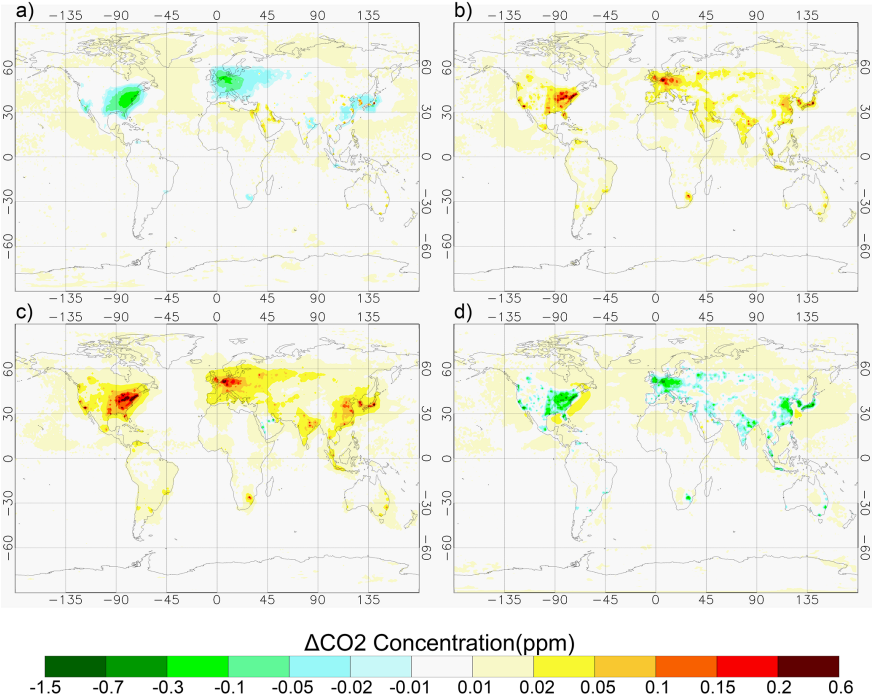

Figure 5. Simulated daily mean surface $FFCO_2$ concentration differences between the WCE and FE emission fields. **(a)** Monday; **(b)** Tuesday and Wednesday; **(c)** Thursday and Friday; **(d)** Saturday and Sunday.

ACPD
15, 20679–20708, 2015

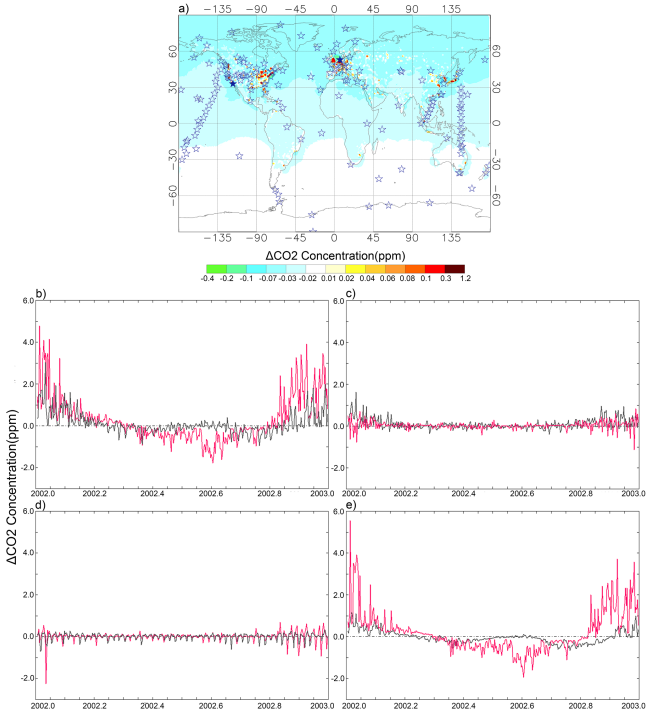

Figure 6. The simulated surface afternoon mean $FFCO_2$ concentration difference (12:00–18:00) between the DCE and FE $FFCO_2$ emissions, and the locations of GlobalView monitoring stations (stars) **(a)**. Daily afternoon mean $FFCO_2$ concentration differences between each cyclic $FFCO_2$ emissions field and FE emissions at two selected GlobalView stations (LJO – gray; LUTDTA – pink); **(b)** for all-time cycle emissions, **(c)** for diurnal-only time cycle emission, **(d)** for weekly-only time cycle emissions and **(e)** for monthly-only time cycle emissions. Solid stars indicate the location of LJO and LUTDTA.

ACPD
15, 20679–20708, 2015

Sensitivity of simulated CO_2 concentration to sub-annual variations

X. Zhang et al.